Gold nanoclusters-loaded hydrogel formed by dimeric hydrogen bonds crosslinking: A novel strategy for multidrug-resistant bacteria-infected wound healing

Zesong Ruan [a], Chunlei Zhang [b,*], Tingwang Shi [a], Zhiyuan Luo [a], Yuna Zhang [b], Zanxia Cao [c,**], Rentai Huang [a], Yunfeng Chen [a,***], Daxiang Cui [b]

[a] *Department of Orthopedic Surgery, Shanghai Institute of Microsurgery on Extremities, Shanghai Jiao Tong University Affiliated Sixth People's Hospital, 600 Yishan Road, Shanghai, 200233, China*
[b] *Institute of Nano Biomedicine and Engineering, Shanghai Engineering Research Center for Intelligent Diagnosis and Treatment Instrument, School of Sensing Science and Engineering, School of Electronic Information and Electrical Engineering, Shanghai Jiao Tong University, 800 Dongchuan Road, Shanghai, 200240, China*
[c] *Shandong Provincial Key Laboratory of Biophysics, Institute of Biophysics, Dezhou University, Dezhou, 253023, China*

ARTICLE INFO

ABSTRACT

Restoring skin integrity after wound infection remains a tougher health challenge due to the uncontrolled antibiotic-resistant pathogens caused by antibiotic abuse. Herein, an injectable hydrogel with dual antibacterial and anti-inflammatory activities composed of gold nanoclusters (GNCs) and carbomer (CBM) is developed for wound dressing to overcome multidrug-resistant infection. Firstly, both experimental investigations and molecular dynamics simulation validate the protonation state of 6-mercaptohexanoic acid (MHA) ligands play an important role in its antibacterial action of GNCs. The self-organizing GNCs-CBM composite hydrogel is then spontaneously cross-linked by the dimeric hydrogen bonds (H-bonds) between the MHA ligands and the acrylic acid groups of CBM. Benefitting from the dimeric H-bonds, the hydrogel becomes thickening enough as an ideal wound dressing and the GNCs exist in the hydrogel with a high protonation level that contributes to the enhanced bactericidal function. In all, by combining bactericidal and immunomodulatory actions, the GNCs-CBM hydrogel demonstrated excellent synergy in accelerating wound healing in animal infection models. Hence, the dimeric H-bonds strengthening strategy makes the GNCs-CBM hydrogel hold great potential as a safe and effective dressing for treating infected wounds.

1. Introduction

Skin wound repair is a vital process after injury during which it will face many challenges in restoring skin integrity, where bacterial infection is one of the trickiest problems to overcome [1,2]. Due to the lack of integrated skin, bacterial and other pathogens have the capacity to initiate the surface colonization on wounds, thereby invading the human body [3,4]. In turn, the open wound with bleeding and exudation provides a breeding ground for bacteria, which aggravates infection and leads wound healing to a slow stage [5]. However, due to a long time of antibiotic abuse, antibiotic-resistant pathogens such as methicillin-resistant *Staphylococcus aureus* (MRSA) have become a global

public health challenge [6,7]. Therefore, efficient and safe antibacterial agents which do not readily develop resistance are urgently needed to deal with infections in the 'post-antibiotic' era [8,9].

Profiting from the unique physicochemical properties, nanomaterials can easily contact or penetrate the bacterial cell membrane, hence fully exerting their strikingly different antibacterial actions [10–12]. In recent years, quantum-sized ultrasmall nanoparticles, such as nanoclusters, have received much attention in biomedicine, catalysis, sensing, and energy conversion [13–16]. Benefitting from the inertness of Aurum, gold nanoclusters (GNCs) have high biocompatibility and hold tremendous promise for clinical antibacterial applications [17–19]. Xie group demonstrated that GNCs can generate intracellular reactive oxygen

---

species (ROS) and destroy bacterial membrane to kill bacteria, which showed that the GNCs were emerging as a wide-spectrum bactericide [20]. Subsequent studies proposed that the antibacterial actions of GNCs can be varied by adjusting ligand modification [21,22]. Recently, we demonstrated that the protonation level of *para*-mercaptobenzoic acid (*p*MBA)-capped GNCs can significantly affect their antibacterial abilities [7]. Therefore, it is of great importance to search for strategies to optimize the antibacterial potency of GNCs.

Compared to Gram-negative bacteria (Gram$^-$), Gram-positive (Gram$^+$) bacteria are bounded by a thick cell wall composed of multiple peptidoglycan layers and negatively charged polyanionic teichoic acids [23,24]. Therefore, decreasing the electrostatic repulsion between the bacterial cell wall and GNCs may improve the antibacterial activity of GNCs against Gram$^+$ bacteria. "Carbomer" is a generic name for a class of cross-linked high molecular weight polymers of acrylic acid [25]. Among them, Carbomer 940 provides excellent gel stability, bioadhesive property, and rheological property, which has been widely used in clinical practice and well-accepted by patients [26]. Currently, there are generally two different thickening mechanisms for carbomer (CBM) hydrogels: neutralization or H-bonding. Neutralization with inorganic or organic bases creates negative charges along the backbone, thereby uncoiling the polymer into an extended structure by the electrostatic repulsion [27]. In addition to the most common neutralization thickening, H-bonding of acrylic acid of polymer molecule to the ingredients causes it to uncoil [28,29]. Based on these theories, we hypothesized that CBM and GNCs could be held together through the intermolecular dimeric H-bonds between the 6-mercaptohexanoic acid (MHA) ligand of GNCs and the acrylic acid groups of CBM. The dimeric H-bonds not only make the CBM hydrogel thickening as a suitable wound dressing, but also keep the ligands of GNCs at a high protonation level to reduce the electrostatic repulsion from the bacterial cell wall and membrane, thereby improving their antibacterial properties [30,31].

Recent research has highlighted the importance of controlling inflammation in treating wound infections [32,33]. Macrophages are an attractive therapeutic target because they participate in the inflammatory response in the progress of wound healing. Macrophages display pro-inflammatory M1 polarization in early stages of infection and then transform into the M2 phenotype for enhanced wound repair later [34]. Persistence of inflammatory induced by M1 macrophages may delay wound healing. Several studies have reported that the gold nanoclusters exerted a critical role in alleviating the inflammatory response by regulating macrophages polarization in rheumatoid arthritis and spinal cord injury [35,36]. Therefore, it is necessary to investigate the immunomodulatory effect of GNCs on macrophages in the progress of infected wound healing, which would provide new insight into the development of wound management strategies.

Herein, with the aid of the dimeric H-bonds between the GNCs and CBM, we prepared the GNCs-CBM hydrogel to inhibit drug-resistance bacterial infection for accelerated wound healing (Scheme 1). After characterizing the rheology, morphology, cell compatibility, antibacterial ability, and immunomodulatory effect of the GNCs-CBM hydrogel dressing, we found that the as-prepared composite hydrogel demonstrated outstanding anti-inflammatory and bactericidal effects *in vitro*. Moreover, the results of wound contraction rate, bacterial count, histopathological examinations, immunohistochemical and immunofluorescence stainings further corroborated the conspicuous acceleration of the infected wound healing *in vivo*. Thus, these results indicated that the GNCs-CBM hydrogels showed great clinical potential as an ideal dressing for infected wound treatment.

2. Materials and methods

2.1. Materials

Gold (III) chloride trihydrate (HAuCl$_4$•3H$_2$O, 99%), sodium borohydride (98%), methanol (99.9%), and ethanol (99.8%) were obtained from Sinopharm Chemical Reagent Co., Ltd. (Shanghai, China). The chemical compounds of 6-mercaptohexanoic acid (MHA, 90%), Carbomer 940 (CAS. NO: 76050-42-5) were purchased from Aladdin Reagent Co., Ltd. (Shanghai, China). Methicillin-resistant *Staphylococcus aureus* (MRSA, ATCC 43300) was obtained from the Department of Microbiology Laboratory, Shanghai Jiao Tong University Affiliated Sixth
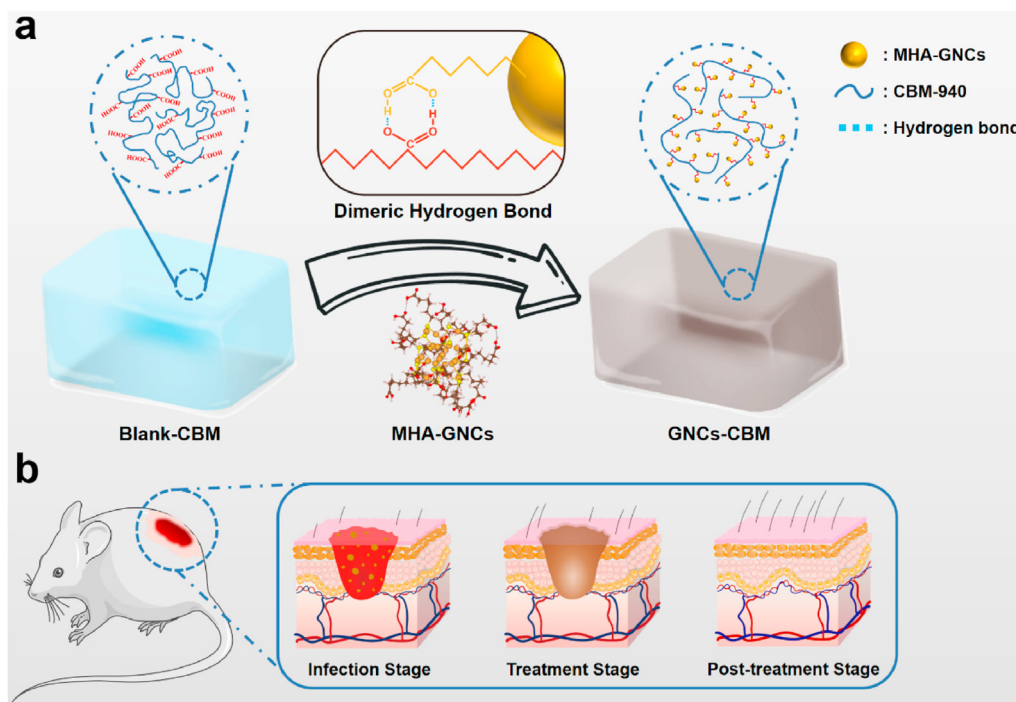
Scheme 1. Schematic diagram illustrating GNCs-CBM hydrogel for multi-drug resistant bacterial infected wound healing. (a) The GNCs-CBM hydrogel was cross-linked by the dimeric H-bonds between MHA-GNCs and CBM-940. (b) The GNCs-CBM hydrogel eradicated multi-drug resistant bacteria and ameliorated the inflammatory microenvironment aroused by infection, which contributed to accelerating wound healing *in vivo*.

People's Hospital. The CCK-8 reagent was purchased from Dojindo Molecular Technologies (Kumamoto, Japan). Rhodamine-labeled phalloidin was purchased from Yeasen Biotechnology Co., Ltd. (Shanghai, China). Tryptic soy broth was purchased from Solarbio Science & Technology Co., Ltd. (Beijing, China). LIVE/DEAD Baclight bacterial viability kit and Baclight bacterial membrane potential kit were purchased from Thermo Fisher Scientific (Waltham, MA, USA). All chemicals were used directly without additional purification.

2.2. GNCs synthesis and characterizations

MHA-GNCs were synthesized according to previously published procedures [7]. The MHA ethanol solution (0.1 M) and $HAuCl_4$ aqueous solution (50 mM) were mixed in water to form the white Au(I)−MHA complexes, which were dissolved in NaOH (1 M, 0.5 mL). Then, $NaBH_4$ solution (150 mM) was added to the mixture and added additional NaOH. Later, the above reaction mixture was stirred quickly for 3 h at room temperature. After adding the NaCl and ethanol, the final product was collected by centrifugation. The product was redissolved in water to get water-soluble $Au_{25}(MHA)_{18}$ nanoclusters. The precipitated nanoclusters were separated by centrifugation at 6000 g for 3 min and washed with double distilled water three times to remove NaCl. The prepared GNCs were then dispersed in water for future experiments.

2.3. Well-tempered metadynamics simulations of molecule−membrane systems

The POPE/POPG (1-palmitoyl-2-oleoyl-*sn*-glycero-3-phosphoethanolamine/phosphoglycerol) (3:1) lipid bilayer was selected as model of Gram-positive bacterial membrane. The bilayer membrane is composed of 24 POPE lipids and 8 POPG lipids. The initial structure and topology of pure lipid bilayer were created by using the CHARMM-GUI Membrane Builder (http://charmm-gui.org/) [37,38]. To obtain equilibrated system, pure POPE/POPG (24:8) lipid bilayer was simulated for 300 ns and the last snapshot was used as the initial structure for molecule-−membrane system. Each molecule−membrane system contains single MHA-COOH or MHA-COO⁻ molecule, which was placed approximately 2 nm above the surface of the bilayer models with parallel orientation.

2.4. Production of GNCs-CBM hydrogel

For preparation of GNCs-CBM hydrogel, 1 g Carbomer 940 was added to 100 mL deionized distilled water to get 1% (w/w) carbomer hydrogel after standing overnight. Then, GNCs (8 mg) were dispersed in hydrogel with gently stirring to get evenly distributed GNCs-CBM hydrogel. Finally, after adjusting the pH of hydrogels with triethanolamine solution, GNCs-CBM hydrogel and Blank-CBM hydrogel (not doped with MHA-GNCs) were stored at 4 °C for future use.

2.5. Characterization of GNCs-CBM hydrogel

The surface morphologies of GNCs-CBM hydrogel and Blank-CBM hydrogel were examined by scanning electron microscopy (JSM-7800F, JEOL, Japan). The rheological properties of GNCs-CBM hydrogel and Blank-CBM hydrogel were analyzed using Discovery Hybrid Rheometer (DHR-2, TA Instruments, USA). The strain amplitude sweep test was conducted with strain amplitude ranging from 0.1 to 100% at a constant frequency of 1 Hz. Frequency sweeps were taken at a constant strain of 1% from 0.1 to 10 Hz.

2.6. Bacterial strains and growth

In our experiments, MRSA was cultured in fresh tryptic soy broth (TSB) medium. A single colony of bacteria was subcultured in TSB at 37

°C and 250 rpm overnight. Bacteria in the logarithmic growth phase was adjusted to obtain a bacteria count of ~10^8 CFU/mL (equivalent to 0.5 McFarland scale) for next use.

2.7. Bacterial colony counting assay

The obtained diluted bacteria liquid was diluted with TSB and mixed with hydrogels. After an incubation of 12 h at 37 °C and 250 rpm, the mixture was diluted 1×10^4-fold with PBS, and 100 μL of the diluted bacterial solution was evenly spread onto the sheep blood agar (SBA) plate. The numbers of bacterial colonies in the plate were quantified after incubation upsetting down at 37 °C for 24 h. And the bacterial counts per milliliter of bacterial solution were calculated. The bacterial viability can be evaluated with the following equation:

$$\text{Bacterial Viability } (\%) = \frac{N_{test}}{N_{ctrl}} \times 100 \tag{1}$$

In this equation, N_{ctrl} is the number of colonies in the control group and N_{test} is the number of colonies in the experimental group. All experiments were performed 3 times.

2.8. Bacterial proliferation curve test

The overnight cultured MRSA liquid was diluted 100-fold with fresh TSB medium at different pHs (pH 5.4 or 7.4) and added to the 96-well plates cultured with or without MHA-GNCs at 37 °C. At different time points (0, 2, 4, 6, 8, 10, and 12 h), the OD_{600} value of each hole was measured to draw the growth curves.

2.9. Bacterial viability live/dead stain

The co-cultured bacterial solution was prepared for staining with LIVE/DEAD Baclight bacterial viability kit. In brief, the centrifuged bacteria were resuspended with 1 mM SYTO-9 and PI which were diluted with PBS. After that, the mix was incubated at 37 °C for 30 min. Next, the collected bacteria were washed and resuspended with PBS. Then, the stained bacterial solution was dropped on the slides, which were viewed with the confocal microscope after mount coverslips.

2.10. Transmission electron microscopy analysis of bacteria

To specify the interaction between GNCs and MRSA, their microstructure analysis was characterized by transmission electron microscopy (TEM). The former bacterial was mixed with hydrogels incubation at 37 °C and 250 rpm for 12 h, and the untreated group was prepared as control. The following steps are carried out in sequence. The samples were fixation in 2.5% glutaraldehyde. Then, the fixed bacterial were washed 3 times with PBS (0.1 M, pH = 7.0) for 15min each, followed postfixed with 1% OsO_4 (osmium tetroxide) for 90 min. The samples were then dehydrated with graded ethanol (30, 50, 70, 80, 90, 95, and 100% [v/v]) for 15 min each. Later, samples were treated with acetone for 20 min, the samples were embedded in epoxy resin to prepare ultrathin sections. After being stained with lead citrate-uranyl acetate by standard methodology, the ultrathin sections were observed in the JEM-2100F field emission TEM (JEOL, Japan).

2.11. Measurement of bacterial membrane potential

Baclight bacterial membrane potential kit was used according to instructions to measure bacterial membrane potential. In brief, 10 μL cultured MRSA were diluted 1:100 in fresh TSB medium and mixed with GNCs-CBM hydrogel cultured for 12 h. Then bacteria were stained with 3,3′-diethyloxacarbocyanine iodide $(DiOC_2(3))$. Carbonyl cyanide 3-chlorophenylhydrazone (CCCP) was added to depolarize the membrane

as the positive control group. Dithiothreitol (DTT) played an anti-oxide role in the test. After incubation for 30 min, the samples were analyzed by flow cytometer (Beckman Coulter, Brea, CA, USA).

2.12. Antibiofilm assay

We diluted the obtained fresh bacteria liquid 100-fold with TSBG (TSB with 0.25% glucose) and the diluted bacteria were added in a confocal dish (diameter 15 mm, Nest) mixed with GNCs-CBM hydrogel. After incubation at 37 °C for 24 h, biofilm formation was determined by crystal violet staining. After discarding the medium, PBS was slightly added to wash away the planktonic bacteria. Biofilms were dried for 20min in the air after being fixed in methanol. Then, the biofilms were stained with 0.5% crystal violet. The stain dye was removed after 20 min and each dish was washed twice with PBS. The stained biofilms were re-solubilized in 33% ethanoic acid and measured at OD_{550} using the microplate reader.

2.13. In vitro cytocompatibility of hydrogel

HUVEC, L929 and RAW 264.7 were cultured in high-glucose DMEM (Sercicebio) containing 10% fetal bovine serum (Gibco) and 1% penicillin/streptomycin (Sercicebio). In the 96-well plates, cells were seeded with a density of 8000 cells per well. After culturing for 24 h, GNCs-CBM hydrogel or the equal volume of Blank-CBM hydrogel was added to the complete growth medium. The cell viability of GNCs-CBM hydrogel was evaluated by CCK-8 assay after culturing 24, 48, and 72 h.

2.14. In vitro influence of hydrogel on cell morphology

After culturing in confocal dishes for 48 h, L929 and HUVEC cells were immunofluorescence stained by FITC-Phalloidin and DAPI to visualize the cell morphology. The adherent cells on the confocal dishes were washed 3 times using PBS and fixed with 4% paraformaldehyde for 15 min. Then, cells were treated with 0.1% Triton X-100 for membrane permeabilization. Finally, the nucleus and cytoskeleton were stained by DAPI and FITC-Phalloidin. Cell morphology was visualized by confocal microscope.

2.15. Hemostatic ability of hydrogels

Fresh blood was obtained from BALB/c mice and heparinized to protect the blood from clotting. Plasma was centrifuged at 1500 rpm at 4 °C for 10 min to isolate red blood cells (RBCs). The obtained RBCs were washed by PBS 3 times until the supernatant became transparent. 100ul of RBC suspension was diluted to 1000 mL in the 1.5 mL EP tube with different treatments. Cellular lysis with Triton X-100 served as the positive control and normal saline served as the negative control. After incubating at 37 °C for 1 h, the mixes were centrifuged at 1500 rpm at 4 °C for 10 min 100 mL of supernatant from each tube was analyzed to verify the hemolysis rate using a microplate reader at 545 nm. The hemolysis rates were calculated as the following equation:

$$\text{Hemolysis Rate } (\%) = \frac{OD_{test} - OD_{neg}}{OD_{pos} - OD_{neg}} \times 100 \qquad (2)$$

In this equation, OD_{test} is the value of the test group, OD_{pos} is the value of Triton X-100 group, and OD_{neg} is the value of the normal saline. All experiments were performed 3 times.

2.16. Animals and treatments

All animal experiments were performed in accordance with the National Institutes of Health Guide for the Care and Use of Laboratory Animals and were approved by Shanghai Jiao Tong University Affiliated Sixth People's Hospital. Six-week-old male BALB/c mice were randomly

divided into three groups and established full-thickness excisional cutaneous wounds (8 mm in diameter) on the back. 10 μL of bacterial suspension with a concentration of 1.0×10^6 CFU/mL were added to the wound. After the liquid was fully absorbed, three groups were respectively treated with normal saline, Blank-CBM hydrogel, and GNCs-CBM hydrogel. Then, animals were covered with Tegader Film (3 M, USA) for 24 h. On day 3, 7 and 12, we observe the infection status and healing progress of the wound and take the photos to record the results. Wound healing rates were calculated as the following equation:

$$\text{Wound healing rate } (\%) = \frac{S_o - S_t}{S_o} \times 100 \qquad (3)$$

where S_o indicated the original size of the wound and S_t represented the size of wounds at the indicated times. At the time of tissue collection (day 7, day 14), animals were euthanasia by injected sodium pentobarbital overdose. The infected wounds with adjacent skin tissues were retrieved for histology stain.

2.17. Bacteria counting of infected tissue

Briefly, equal amounts of wound tissues (1 g) of each group were prepared with a tissue homogenizer and diluted 100 times using PBS. Then, 100 μL of diluted homogenates was used for plating and subsequent counting.

2.18. Histological analysis

The collected specimens were fixed with 4% paraformaldehyde for 24 h, and then tissues were embedded in paraffin and sectioned serially at 5 μm. These slides were subjected to H&E staining for routine analysis. As for some special analysis, Giemsa staining was used to verify the residual bacteria in sections. Immunohistochemical staining of TNF-α and CD31 were used to measure inflammatory response and neovascularization level. Immunofluorescence staining of CCR7 and Arg-1 were used to examine macrophages polarization [39,40]. Immunofluorescence staining of CD31 and α-SMA were used to examine the level of angiogenesis [41]. The application of Masson's staining could evaluate the level of collagen deposition. The sections were observed with an inverted microscope (DMi8, Leica Microsystems, German) for quantitative analysis.

2.19. Statistical analysis

All data were obtained from at least three replicate experiments and analyzed with the Student's *t*-test in the GraphPad Prism 8.0.1 (La Jolla, CA, USA). The data were shown as mean ± SD ($n = 3$ or 5), and a difference of *$p < 0.05$ was considered statistically significant. All error bars represented the standard deviations.

3. Results and discussion

3.1. Evaluation of bactericidal properties of MHA-GNCs

Firstly, the MHA-GNCs were synthesized according to previously published procedures [7]. As shown in the UV–vis spectrum (Fig. 1a), the MHA-GNCs demonstrated the characteristic absorption peaks of $Au_{25}(MHA)_{18}$ nanoclusters with a broader band at 670 nm and two shoulder peaks at 400 and 450 nm [42]. Furthermore, by electrospray ionization mass spectrometry (ESI-MS), we observed the most intense peak at $m/z \sim 2523$ in the range of 2000–3000, which can be assigned to $[Au_{25}(MHA)_{18}\text{-}3H^+]^{3-}$ species (Fig. 1b). The ESI-MS result was consistent with the molecular weight of $Au_{25}(MHA)_{18}$ nanoclusters. TEM image demonstrated that the average core size of MHA-GNCs was around 1.8 nm (Fig. 1c). The protonation/deprotonation state of the ligands at different pH values was additionally confirmed with the
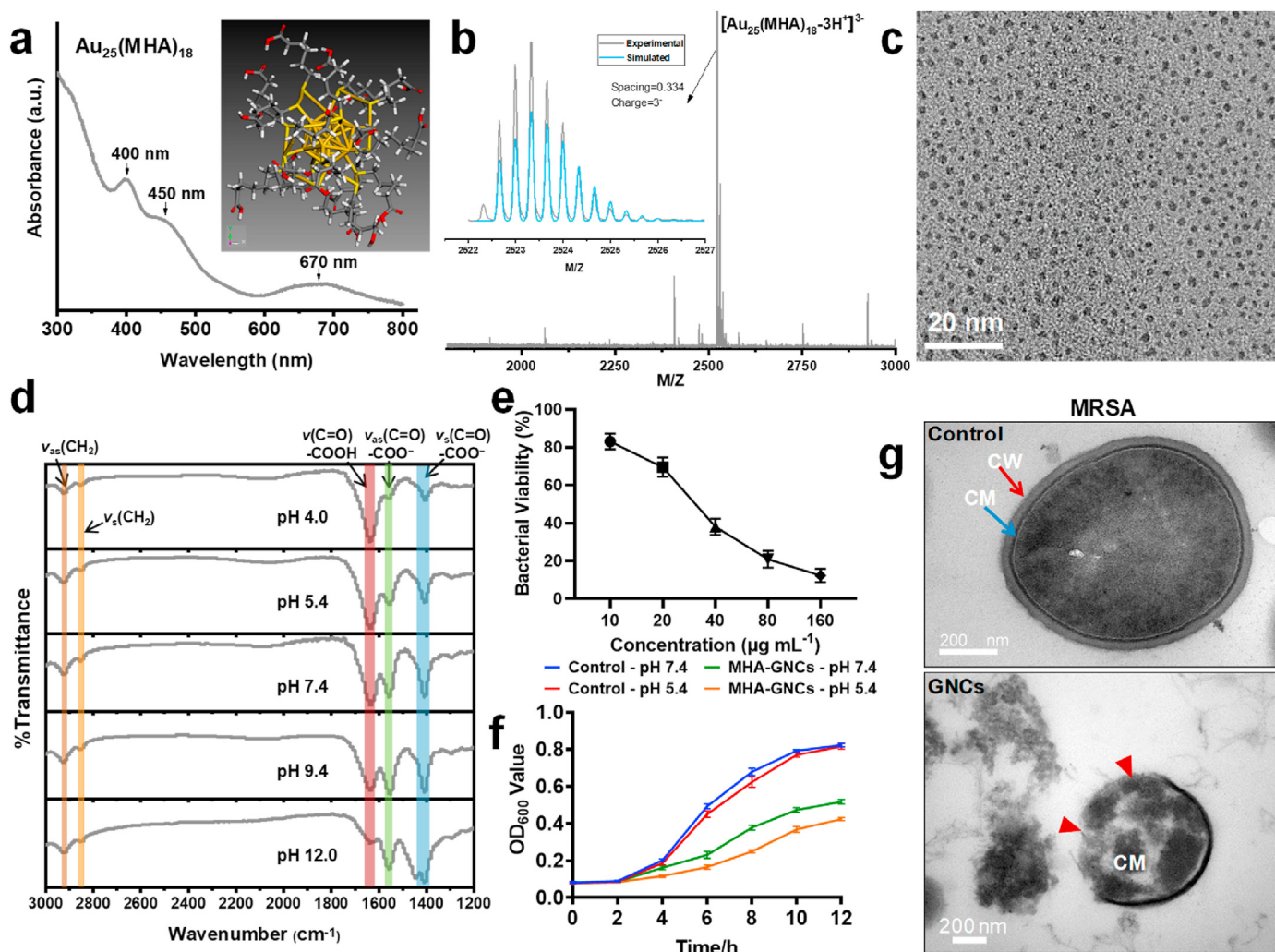
Fig. 1. Characterization and bactericidal properties of MHA-GNCs. (a) UV–vis spectrum of the $Au_{25}(MHA)_{18}$ nanoclusters. Inset is the diagram depicting the molecular structure of $Au_{25}(MHA)_{18}$ nanocluster. (b) Negative-mode ESI-MS spectrum of $Au_{25}(MHA)_{18}$ nanoclusters. Inset is the simulated and experimental isotope patterns for the 3⁻ species. (c) TEM image of MHA-GNCs. Scale bar, 50 nm. (d) pH-dependent FTIR spectra of MHA-GNCs in solid phase. Dashed red, green, and blue bands stand for the positions of protonated –COOH groups, v_{as} and v_s stretching modes of deprotonated –COO⁻ groups, respectively. Dashed orange bands represent the stretching modes of –CH₂ groups. (e) Bacterial viability of MRSA in presence of MHA-GNCs with different concentrations. (f) Proliferation curves of MRSA cultured with or without MHA-GNCs at different pHs (pH 5.4 or 7.4). (g) Ultrastructure observation of MRSA. Red and blue arrows point at the cell wall (CW) and cytoplasmic membrane (CM), respectively. Red triangles indicate the cells with broken CW and CM. Scale bar, 200 nm.

Fourier-transform infrared (FTIR) spectroscopy, the protonation state in aqueous solution was preserved when the MHA-GNCs was dried. As shown in Fig. 1d, the reliably identified of a strong, broad band close to 1634 cm^{-1}, assigned to the C=O stretching vibration mode of –COOH groups, is indicative of the protonated carboxylic acid groups of MHA ligand when the MHA-GNCs at pH 4.0. With increasing pH values, the absorption of –COOH groups became weaker, which was accompanied by the strikingly increase in the asymmetric (v_{as}) and symmetric (v_s) stretching modes of the –COO⁻ group at 1554 and 1404 cm^{-1}, respectively [43,44]. In the fully deprotonated states of MHA-GNCs at pH 12.0, this signal attributed to –COOH groups was only faintly observed. The band at 2926 and 2851 cm^{-1} associated with the v_{as} and v_s stretching vibrations of CH₂ groups of MHA ligands [45].

The protonation/deprotonation state of the ligands determines the macroscopic amphiphilic nature and surface charge of the MHA-GNCs, which would affect their bactericidal performance. In this study, we employed the MRSA strain, one of the most common obstinacy bacteria in infected wounds, to evaluate the antibacterial activity of GNCs. The GNCs exhibited antibacterial capability even at a low concentration (Fig. 1e). Besides, it is necessary to verify whether keeping GNCs at a

higher protonation level with less negative charge is beneficial for their antibacterial activities. To test our hypothesis, bacteria were cultured with GNCs in TSB mediums at two different pH values (5.4 and 7.4), achieving two different protonation levels (high and low) of MHA ligands for bactericidal tests [46]. Interestingly, proliferation curves demonstrated that the antimicrobial activity of GNCs against MRSA at acidic conditions (pH 5.4) is much higher than that found at neutral pH (pH 7.4) (Fig. 1f), most likely due to the increased hydrophobicity with more ligands protonated [47], which is in accord with the protonation states of ligands at different pH values revealed by the FTIR spectra in Fig. 1d. Therefore, keeping the MHA ligands of GNCs at a high protonation level will help to exert the bactericidal effects. Furthermore, visual inspection of GNCs-induced MRSA cellular damage was evaluated by TEM. As shown in Fig. 1g, compared to the untreated MRSA with a smooth and intact cytoplasmic membrane surrounded by thick cell walls, the MRSA treated with GNCs appeared visibly lysed with damaged cell wall and membrane.

To more precisely establish the essential role of carboxylic groups in the antimicrobial activity of GNCs, we performed metadynamics simulations and molecular dynamics simulations to elucidate the molecular
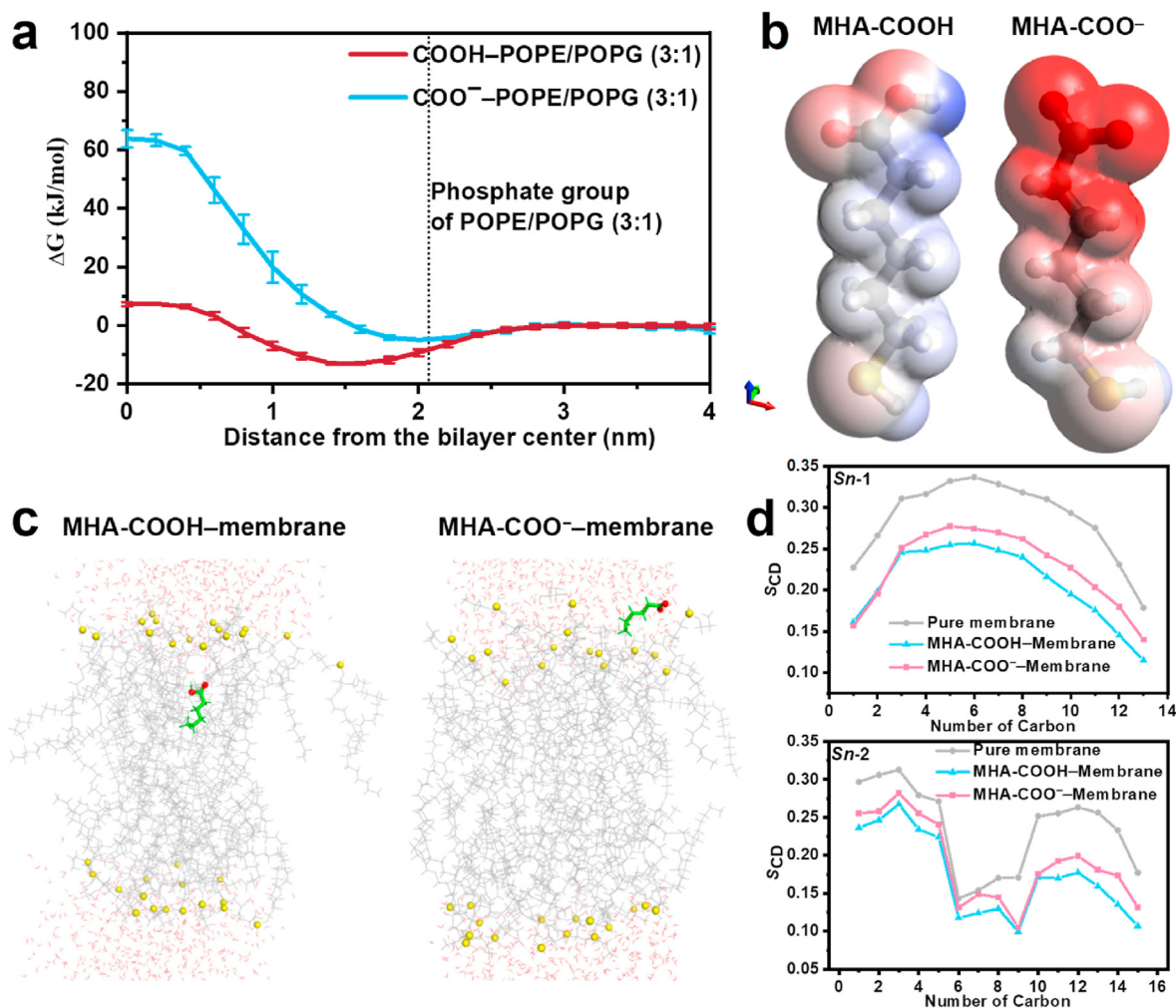
Fig. 2. Molecular simulation study of the molecular basis of antibacterial activity. (a) One dimensional free energy for MHA-COOH and MHA-COO⁻ as a function of the *z*-directional distance between the center of peptide and the center of bilayer. The free energy value is set zero in the water phase. (b) ESP-mapped electron density of MHA-COOH and MHA-COO⁻ (red, negative; blue, positive), respectively. (c) Snapshots of MHA-COOH and MHA-COO⁻ at the energy minimum of the bilayer. In the snapshot, MHA-COOH and MHA-COO⁻ are shown with green sticks and the oxygen atoms are shown as red spheres. The lipid phosphorus atoms are shown as yellow spheres. The lipid tails are shown as thin gray lines. Water is shown as red (oxygen) and gray (hydrogen) cylinders. (d) Deuterium order parameter (S_{CD}) profiles calculated for the *Sn*-1and *Sn*-2 acyl chains in the pure bilayer and the MHA molecule−bilayer systems.

basis of this mechanism. For computational simplicity, only the molecule (MHA)-membrane systems were used. Fig. 2a shows the one-dimensional free energy (ΔG) of translocating two MHA molecules into the POPE/POPG (3:1) bilayer (model of Gram-positive bacterial membranes) along the *z*-directional distance between the center of the molecule and that of the bilayer. As shown in the free energy profiles (FEPs), **o**ne main difference between these two molecules is the location of the free energy minimum. The energy minimum of the MHA-COOH is located around 1.4 nm with the value of −13.0 kJ/mol. Comparatively, the energy minimum of the MHA-COO⁻ is located around 2.2 nm with the value of −4.9 kJ/mol. The binding free energies of MHA–COOH–bilayer and MHA-COO⁻-bilayer for two molecules at the energy minimum are calculated by using g_mmpbsa [48]. The calculated binding free energies of MHA-COOH–bilayer and MBA-COO⁻–bilayer are −38 ± 8 and 118 ± 34 kJ/mol (Table S1), respectively. To further explore these results, the binding free energy was decomposed into individual energies. The sum of *van der Waals* interactions and nonpolar solvation energies of MHA-COOH–bilayer and MHA-COO⁻–bilayer are −62 ± 9 and −9 ± 2 kJ/mol (Table S1), respectively. However, the electrostatic contribution (the sum of electrostatic interaction energy and polar solvation energy) of

MHA-COOH–bilayer and MHA-COO⁻–bilayer are 24 ± 8 and 127 ± 25 kJ/mol, respectively. The electrostatic contribution was more unfavorable for MHA-COO⁻–bilayer system than MHA-COOH–bilayer system.

As indicated in Fig. 2b, differences in electrostatic potential (ESP)-mapped electron density of the carboxyl-terminal ligands highlight the importance of protonation state of the ligands. Molecular dynamics simulations further revealed that the short-range H-bonding play vital roles in steering the MHA ligand toward the negatively charged membranes (Fig. 2c). Bacterial membranes have been identified as the major targets for the activity of most antibacterial molecules. Therefore, the deuterium order parameters (S_{CD}) of the acyl chains were calculated in both pure POPE/POPG (3:1) lipid bilayers and the molecules−membrane systems. As depicted in Fig. 2d, the order of acyl chains in all the molecules−membrane systems was decreased compared to pure POPE/POPG (3:1) membrane. For the simulations of molecules at the energy minimum, there was a big difference of the S_{CD} between MHA-COOH and MHA-COO⁻. The order is MHA-COO⁻ < MHA-COOH. The results indicated that MHA-COOH can induce further disordering relative to the MHA-COO⁻.

3.2. Preparation, characterization, and biocompatibility assessment of GNCs-CBM hydrogel

After synthesizing the MHA-GNCs, a simple and convenient approach has been developed to prepare injectable GNCs-CBM hydrogel *via* self-organizing blend of GNCs and CBM hydrogels. The nanocomposite hydrogel was more viscous and possessed brown color due to the content of GNCs (Fig. 3a). The scanning electron microscope (SEM) images of the freeze-dried GNCs-CBM hydrogel showed that electron-dense rough aggregates were evenly distributed on the porous wall of the hydrogel, but the blank carbomer (Blank-CBM) hydrogel was smooth without any aggregates (Fig. 3b), which indicated that GNCs aggregates were uniformly distributed within the hydrogel. Rheological experiments were carried out to assess the viscosity change of hydrogels. The result of amplitude sweep test demonstrated the higher storage modulus (G') than loss modulus (G'') (Fig. 3c), which confirmed the gel-like viscoelastic behavior of GNCs-CBM hydrogel. As shown in Fig. 3d, the GNCs-CBM hydrogel displayed higher modulus than the Blank-CBM hydrogel, indicating the formation of a stronger hydrogel. Thus, it is reasonable to assume that the presence of carboxylic groups in the GNCs could bring about additional dimer H-bonding interactions with hydrogel, which affects the final rheological properties of the hydrogel.

Good biocompatibility of hydrogels is the primary prerequisite for their clinical applications. The biocompatibility of the GNCs-CBM hydrogel was evaluated in HUVEC (vascular endothelial cells), L929 cells (fibroblasts) and RAW264.7 cells (macrophages) using CCK-8 cytotoxicity assay. The results demonstrated that insignificant toxicity of GNCs-CBM hydrogel was observed with Balnk-CBM hydrogel, GNCs-CBM hydrogel or GNCs (Fig. S1). Subsequently, hemolysis experiments were carried out to evaluate the blood compatibility of hydrogels. After co-incubating for 1 h, insignificant hemolysis of fresh blood occurred in all groups (Fig. S2). Furthermore, tetramethyl rhodamine isothiocyanate (TRITC) phalloidin staining showed that cells could attach to the surface with typical normal morphology when treated with GNCs-CBM hydrogel, where no obvious changes of actin cytoskeleton could be found (Fig. S3).

Besides, the expression of HUVEC activation markers (including P-and E-selectin), which contribute significantly to neutrophil recruitment and promote the vicious circle of inflammation [49,50], were evaluated to explore the impact of different treatments on the functions of HUVEC. The quantitative real-time PCR (qRT-PCR) results in Fig. S4 demonstrated that the MHA-GNCs and GNCs-CBM hydrogel induced the down-regulations of *SELP* and *SELE* mRNA expressions in HUVEC, indicating the limited inflammatory activation in the endothelial cell. Hence, GNCs-CBM hydrogel exhibited outstanding biocompatibility.

3.3. In vitro antibacterial activity of GNCs-CBM hydrogel

To confirm the *in vitro* antibacterial activity of GNCs-CBM hydrogel, the colony formation counts in plates were recorded with dilution separation methods (Fig. 4a). The Blank-CBM hydrogel showed no bactericidal activity (Fig. 4b). By contrast, the GNCs-CBM hydrogel demonstrated an excellent bactericidal activity with only $8.89 \pm 1.11\%$ bacteria were survival, which was even more effective than only GNCs treatment ($17.13 \pm 2.24\%$). Furthermore, the live/dead staining was performed with live bacteria stained green (SYTO9) and dead bacteria stained red (propidium iodide, PI). As shown in Fig. 4c, the GNCs-CBM hydrogel group exhibited widely spread red fluorescence. In contrast, the control group and Blank-CBM group showed intense green fluorescent signal. Then, the stained bacteria were further quantitatively analyzed with flow cytometer (Fig. 4d). The results showed that PI-positive rates of the groups were $0.53 \pm 0.11\%$ (Blank-CBM), $88.83 \pm 1.40\%$ (GNCs-CBM), $80.98 \pm 1.44\%$ (GNCs), respectively (Fig. 4e). Altogether, these data demonstrated the enhanced bactericidal activity of GNCs-CBM hydrogel. It is well known that biofilm was mainly composed of the self-secreted extracellular matrix, which acted as the parclose for inhibiting antibiotic penetration and induced the bacteria rapidly develop drug-resistance [51]. We next evaluated the biofilm inhibition and elimination effects of these hydrogels by using crystal violet staining assay (Fig. 4f). The OD_{550} values indicated the amounts of biofilms biomasses (Fig. 4g) [52]. Among all the groups, the GNCs-CBM hydrogel
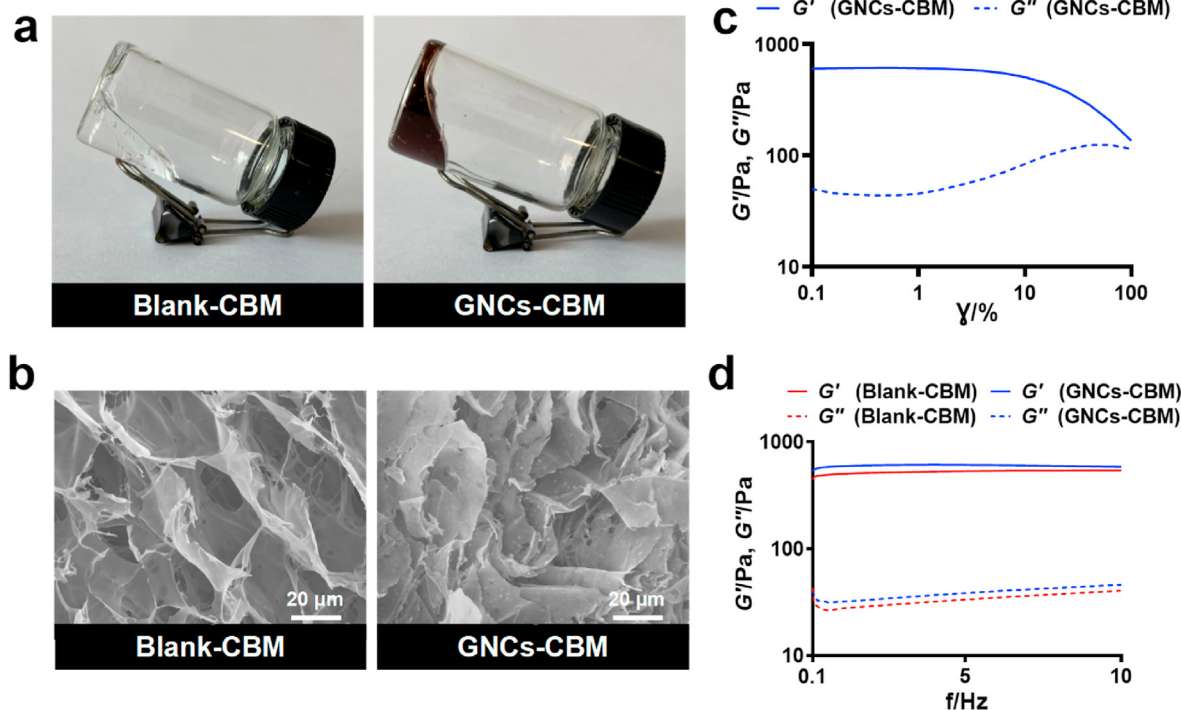

Fig. 3. Characterization of GNCs-CBM hydrogel. (a) Representative photographs of Blank-CBM hydrogel and GNCs-CBM hydrogel that placed after 1 h. (b) SEM images of freeze-dried Blank-CBM hydrogel and GNCs-CBM hydrogel. Scale bar, 20 μm. (c) Amplitude sweep test of GNCs-CBM hydrogel. (d) Frequency sweep test of Blank-CBM hydrogel and GNCs-CBM hydrogel.
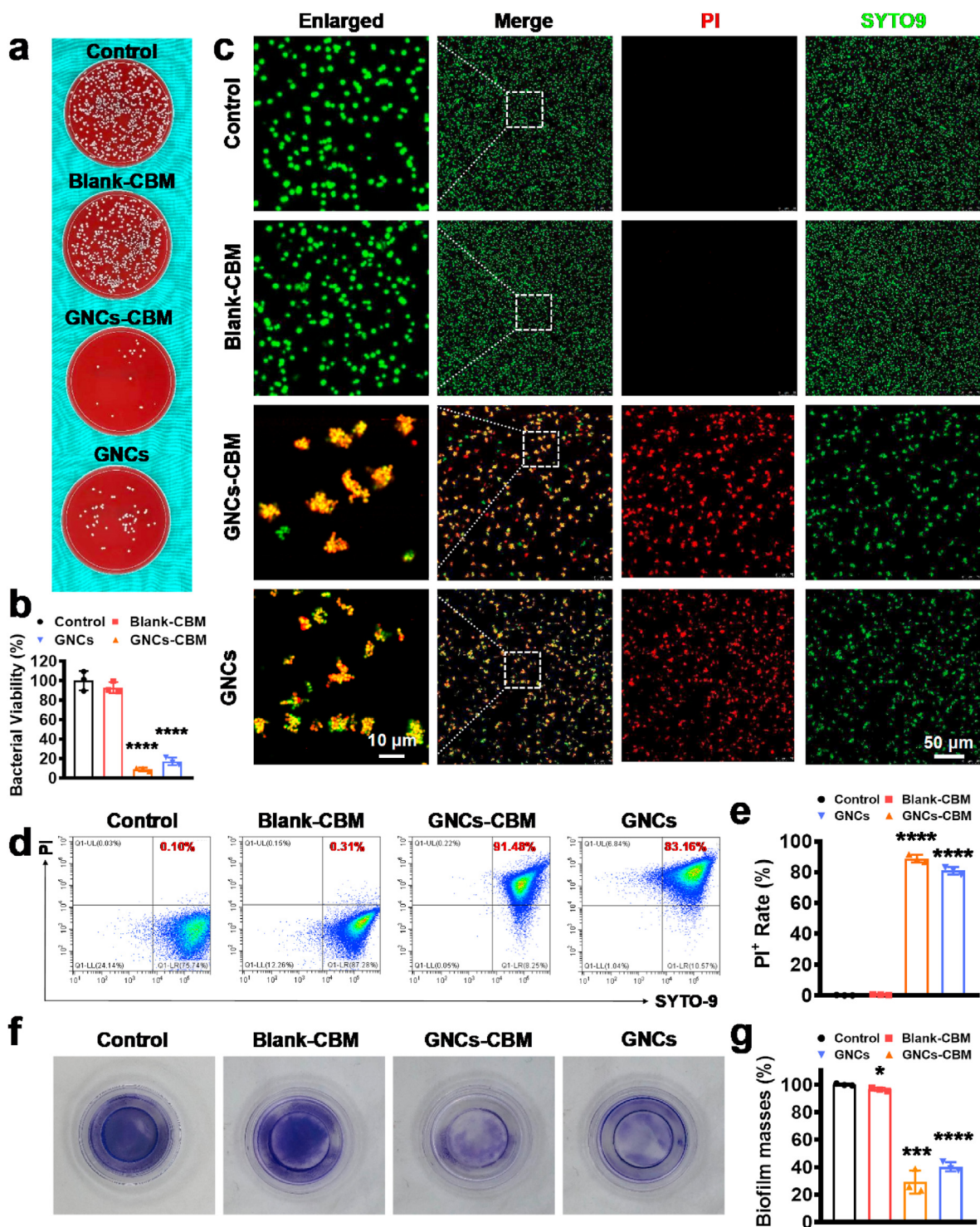
Fig. 4. Bactericidal study of GNCs-CBM hydrogel *in vitro*. (a) Digital photos of bacterial colonies grown on sheep blood agar plates with different treatment groups. (b) Quantification of the numbers of CFU in (a). (c) Confocal micrographs of the MRSA treated by different groups. PI (red): dead bacteria, SYTO9 (green): live bacteria. Scale bars, 10 μm, 50 μm for enlarged images. (d) Flow cytograms of PI and SYTO9 co-staining bacteria after treatment. (e) Quantitative PI-positive bacteria rate analysis of (d). (f) Digital photos of the biofilms (stained by crystal violet) with different treatment groups. (g) Dissolving the stained biofilm in (f) for quantification of absorbance at 550 nm. The treated bacteria in (c, d) were co-stained by PI and SYTO9 for flow cytogram assay and quantitative PI $^+$ rate. $n = 3$, $*p < 0.05$; $**p < 0.01$; $***p < 0.001$; $****p < 0.0001$.

group exhibited the lowest OD_{550} values (29.17 $\pm$ 4.88%), which demonstrated the best antibiofilm activity. Thus, the combination of CBM hydrogel and GNCs showed a synergistic antibiofilm effect.

To clarify the bactericidal mechanism of GNCs-CBM hydrogel, we subsequently validated the membrane destruction of GNCs-CBM

hydrogel *via* testing bacterial membrane potential [53]. The cyanine dye $DiOC_2(3)$ could exist in all bacterial cells and emit green fluorescence. While, due to the formation of aggregates in the polarized bacterial membrane, this dye exhibits red-shifts in the fluorescence emission in intact bacteria. CCCP played as positive control which could depolarize

the membrane potential, while DTT played as a reducing reagent which could reverse the effects of produced ROS [54]. As shown in Fig. S5, the GNCs-CBM group presents an obvious membrane potential decrease similar to that of the CCCP group, which indicated the destruction of membrane and was congruent with our above results. When bacteria were treated with DTT and GNCs-CBM hydrogel, the membrane potential was recovered due to the reducing environment created by DTT. Thus, GNCs-CBM hydrogel-induced ROS generation has been one of the main reasons for the antibacterial effect.

3.4. In vitro immunomodulatory effects of GNCs-CBM hydrogel

We subsequently investigate the effects of the GNCs-CBM hydrogel to modulate the phenotype and function of macrophages using RAW 264.7. As shown in Fig. 5a, Western blotting analysis was used to detect influence in the expression of polarization relevant proteins such as CD86 (M1 phenotype marker) and CD206 (M2 phenotype marker) [55]. The relative quantitative results in Fig. 5b demonstrated that the expression of CD86 was inhibited while the expression of CD206 was activated after the GNCs-CBM hydrogels treatment, indicating a shift toward M2 macrophage polarization. These results were consistent with our qRT-PCR results (Fig. S6) and flow cytometry result (Fig. 5c). In addition,

we verified the potential of the composite hydrogels on the polarization of macrophages by immunofluorescence staining with another pair of markers, CCR7 (M1 marker) and Arg-1 (M2 marker). As shown in Fig. 5d, the GNCs-CBM group showed higher expression of CCR7 (green) and lower expression of Arg-1 (red) than the Blank-CBM group, indicating the critical regulatory function of composite hydrogel in inducing anti-inflammatory M2 polarization.

Subsequently, based on the pivotal role of M2-polarized macrophages in wound angiogenesis, we detect the expression level of proangiogenic cytokines, such as VEGF and PDGF [56,57]. As shown in Fig. S7, The *Vegfa* and *Pdgfb* gene expression in the MHA-GNCs group and the GNCs-CBM group were notably upregulated in comparison with the control group and the Blank-CBM group, which indicated that MHA-GNCs can promote angiogenesis. These results demonstrated the GNCs-CBM hydrogel exerted anti-inflammatory and immunomodulatory effects.

3.5. In vivo anti-infection and wound healing effects of GNCs-CBM hydrogel

Bacterial infected wounds are common after injury due to the lack of the protection of skin. In this research, we designed the GNCs-CBM
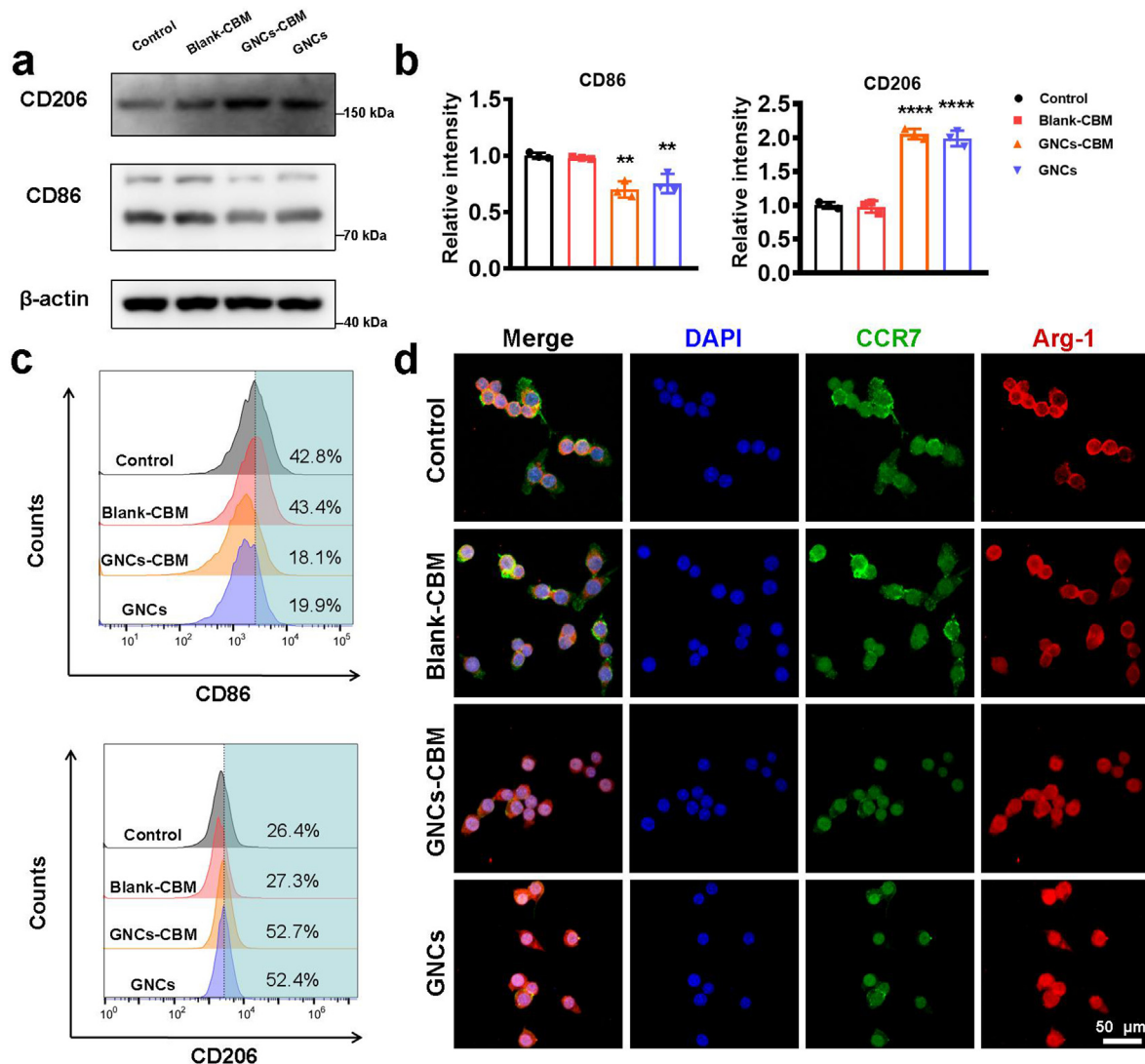

Fig. 5. The immunomodulatory effects of GNCs-CBM hydrogel on macrophages. (a) Western blotting images of the macrophage polarization markers (CD86 and CD206). (b) Relative quantitative analysis of CD86 and CD206. (c) The mean fluorescence of the CD86 and CD206 was measured by flow cytometry. (f) Representative confocal micrographs of the RAW264.7 cells under different treatments. CCR7 (green, M1), Arg-1 (red, M2). Scale bar, 50 μm n = 3, **p < 0.01; ****p < 0.0001.
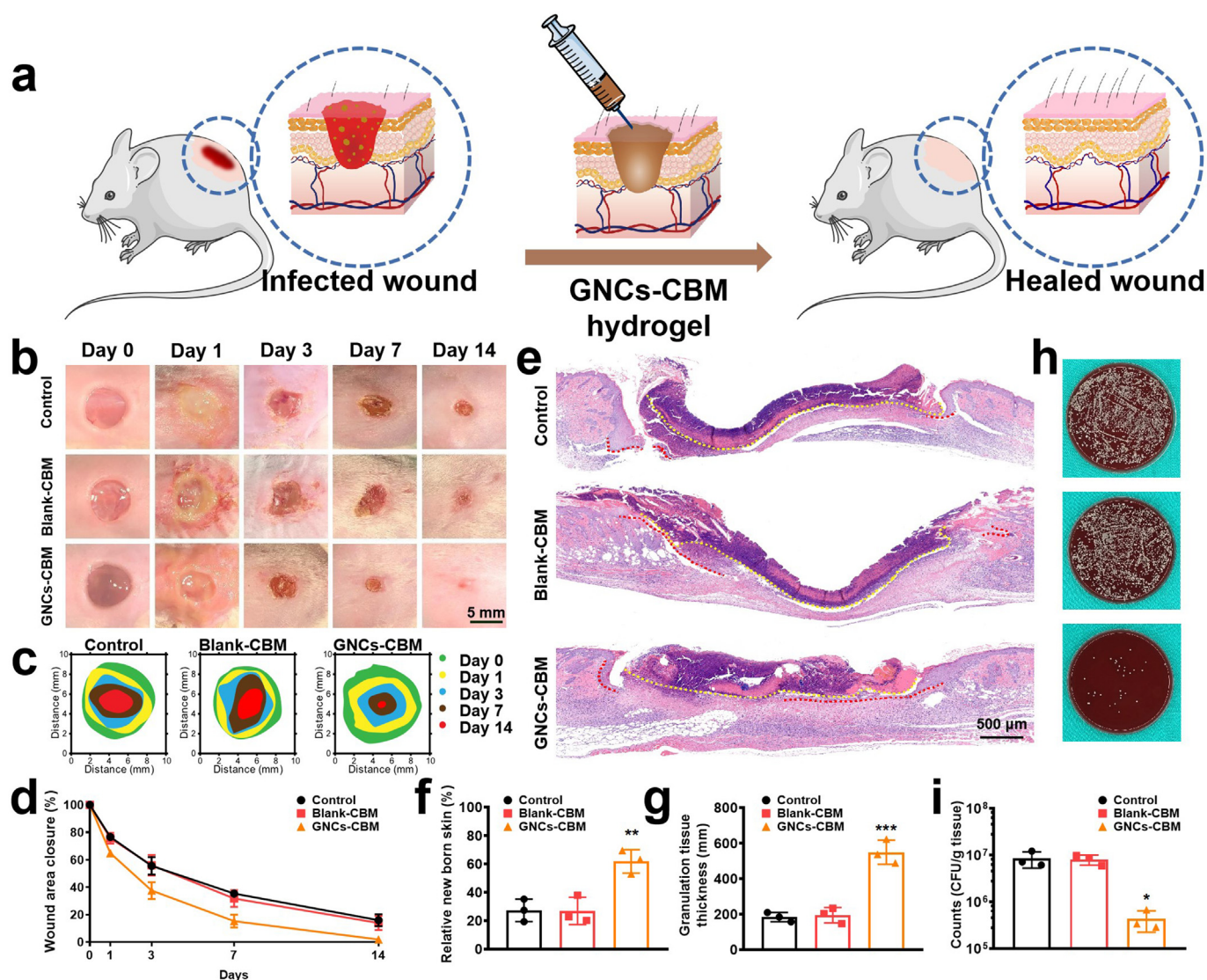
Fig. 6. GNCs-CBM hydrogel promotes the repairing of the infected wounds *in vivo*. (a) Schematic diagram illustrating the treatment process of GNCs-CBM hydrogel that promotes the wound healing. (b) Representative macroscopic digital images of wound site on day 0, 1, 3, 7, and 14 post-infection. Scale bar, 5 mm. (c) Schematic illustration of wound healing profile. (d) The wound area closure rates of different groups. (e) H&E staining of infected wounds on day 7. The yellow lines indicate the scar and the red lines indicate the newborn epidermis. Scale bar, 500 μm. (f) The relative area of newborn epidermis under scab on day 7. (g) Quantification of the granulation tissue formation in samples harvested on day 7. (h) Digital photos of bacterial colonies grown on sheep blood agar plates of wound tissues after homogenates. (i) Quantification of the numbers of CFU in (h). $n = 3$, $*p < 0.05$; $**p < 0.01$; $***p < 0.001$.

hydrogel as wound dressing for preventing and treating wound infection. To verify the therapeutic effects *in vivo*, we tested the performance of the hydrogels in infected wound healing in BALB/c mice (Fig. 6a). At the indicated time point (day 0, 1, 3, 7, and 14), the healing progress of the infected wounds was recorded by digital photos (Fig. 6b). The GNCs-CBM group presents the most obvious accelerated wound closure result by comparing the relative wound areas (Fig. 6c). It is worth noting that the areas of wound contraction treated by GNCs-CBM hydrogel was 15.31 ± 2.68% on day 7, but the control group even took twice as long to achieve similar results (16.01 ± 2.53%, on day 14) (Fig. 6d). At the early (day 7) and late (day 14) post-treatment points, the cutaneous samples around the wound were stained for further analyses.

As shown in Fig. 6e, the H&E staining result indicated that the damaged dermis and epidermis were regenerated under the scab. Among all the groups, the wound treated with GNCs-CBM hydrogel (61.87 ± 4.78%) presented a significantly wider range of epithelial proliferation under the scab than that of control (27.30 ± 4.59%) and Blank-CBM

group (26.95 ± 5.55%) (Fig. 6f). Granulation tissue is mainly composed of fibroblasts and capillaries where fibroblasts are involved in tissue repair post-injury and capillaries delivered growth factors. The thickness of the granulation tissue in the GNCs-CBM group (549.3 ± 39.35 μm) was much thicker than that of other groups (183.91 ± 15.24 μm, control group and 194.90 ± 25.33 μm, Blank-CBM group) (Fig. 6g), which is a sign of better wound healing. Besides, bacteria in sections were monitored by Giemsa staining, which revealed that bacteria were only scarcely seen in the GNCs-CBM group (Fig. S8). Moreover, the variation tendency of CFU counts of wound tissues homogenates was consistent with the results of Giemsa staining (Fig. 6h). Quantitatively, the GNCs-CBM group exhibited an average 20-fold decrease in CFU when compared with the Blank-CBM group (Fig. 6i).

This fast wound healing may be attributed to the excellent antibacterial effect of GNCs-CBM hydrogel. Additionally, to investigate the *in vivo* safety of GNCs-CBM hydrogel, the main organs of mice were collected and sliced for H&E staining at the end of the experiment. The

results showed that there was no obvious tissue damage or inflammatory lesion observed in all major organs (Fig. S9). Thus, GNCs-CBM is a highly promising wound dressing with excellent biocompatibility.

3.6. In vivo therapeutic evaluation with GNCs-CBM hydrogel

Subsequently, we evaluated the level of inflammation and angiogenesis in the wound area after treatment. The expression levels of tumor necrosis factor-alpha (TNF-α), a critical inflammatory mediator during wound healing, were evaluated by immunohistochemical assay (Fig. 7a). The staining result in Fig. 7b showed that the GNCs-CBM group had the lowest expression level of TNF-α among all the groups, which suggested minimal inflammatory response in GNCs-CBM group. Furthermore, the extent of neovascularization was assessed by staining with CD31, a pan-endothelial marker to evaluate the degree of vessel formation. (Fig. 7c). The result demonstrated that the new-born microvascular area ratio of GNCs-CBM group was more than 10-fold higher than those of all other groups (Fig. 7d). Thus, due to the lack of therapeutic neovascularization, the Blank-CBM group and the control group showed impaired wound healing process.

The suppressed inflammatory response and accelerated angiogenesis in the wound after treatment reminded us the immunomodulatory effects of GNCs-MHA hydrogel on macrophages polarization. Generally, macrophages undergo a transition from a pro-inflammatory 'M1' state to an anti-inflammatory 'M2' state in the wound healing progress [58]. The appropriate timing of inflammation and its resolution in the wound healing response is essential to proper wound closure, with persistent inflammation inducing delayed wound healing [59]. Thus, to investigate the possible effect of GNCs-CBM hydrogel on macrophage polarization *in vivo*, wound tissues were double stained with CCR7 (green) and Arg-1(red) immunofluorescence to assess the M1/M2 macrophage polarization pattern. As shown in Fig. S10, the proportion of M2 macrophages was significantly improved by GNCs-CBM hydrogel relative to the other groups on day 3, which means that the wound healing has converted the inflammatory phase into the repair phase at an early time. In addition, the GNCs-CBM group exhibited extensive M2 macrophages infiltration compared with the control group and the Blank-CBM group on day 7 (Fig. 7e). The quantitative results in Fig. 7f supporting our previous conclusion that the immunomodulatory effects of the GNCs-CBM hydrogel played a key role in the wound healing process.

Thus, the outstanding wound healing properties of GNCs-CBM hydrogel can be explained by these two factors. On one hand, GNCs-CBM hydrogel with excellent bactericidal property effectively reduces the level of inflammation caused by bacteria. On the other hand, we
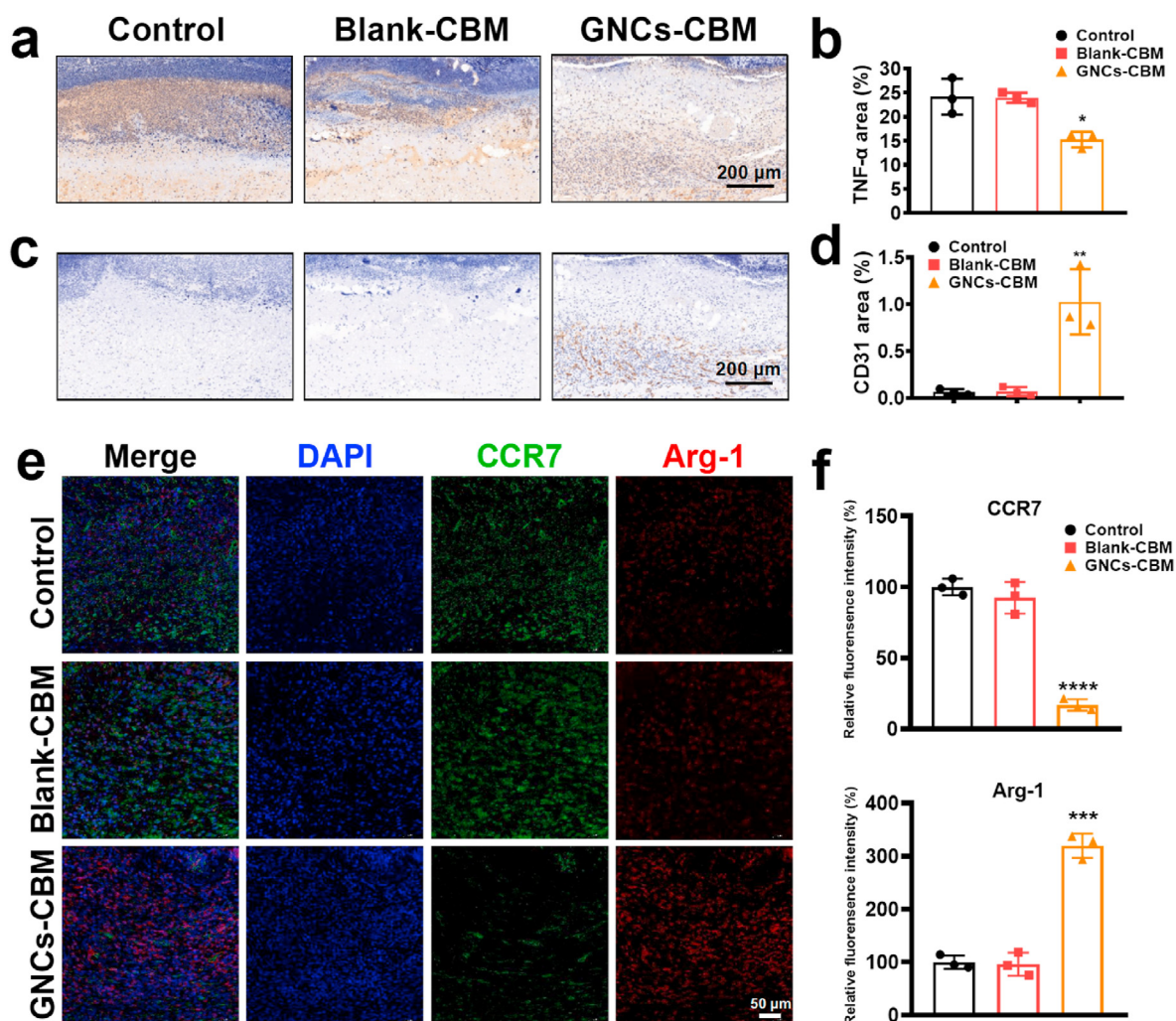

Fig. 7. GNCs-CBM hydrogel inhibits inflammation microenvironment and promotes the formation of granulation tissues at early stages *in vivo*. (a) Immunohistochemical staining images of proinflammatory factors TNF-α in infected wounds on day 7. Scale bar, 200 μm. (b) Quantification of the TNF-α-positive areas. (c) Immunohistochemical staining images of CD31 in granulation tissues on day 7. Scale bar, 200 μm. (d) Quantification of the CD31-positive areas. (e) Representative immunofluorescence images of CCR7 and Arg-1 double-stained sections from different groups on day 3. Scale bar, 50 μm. (f) Quantification of the fluorescence intensity of CCR7 and Arg-1. $n = 3$, $*p < 0.05$; $**p < 0.01$; $***p < 0.001$; $***p < 0.0001$.
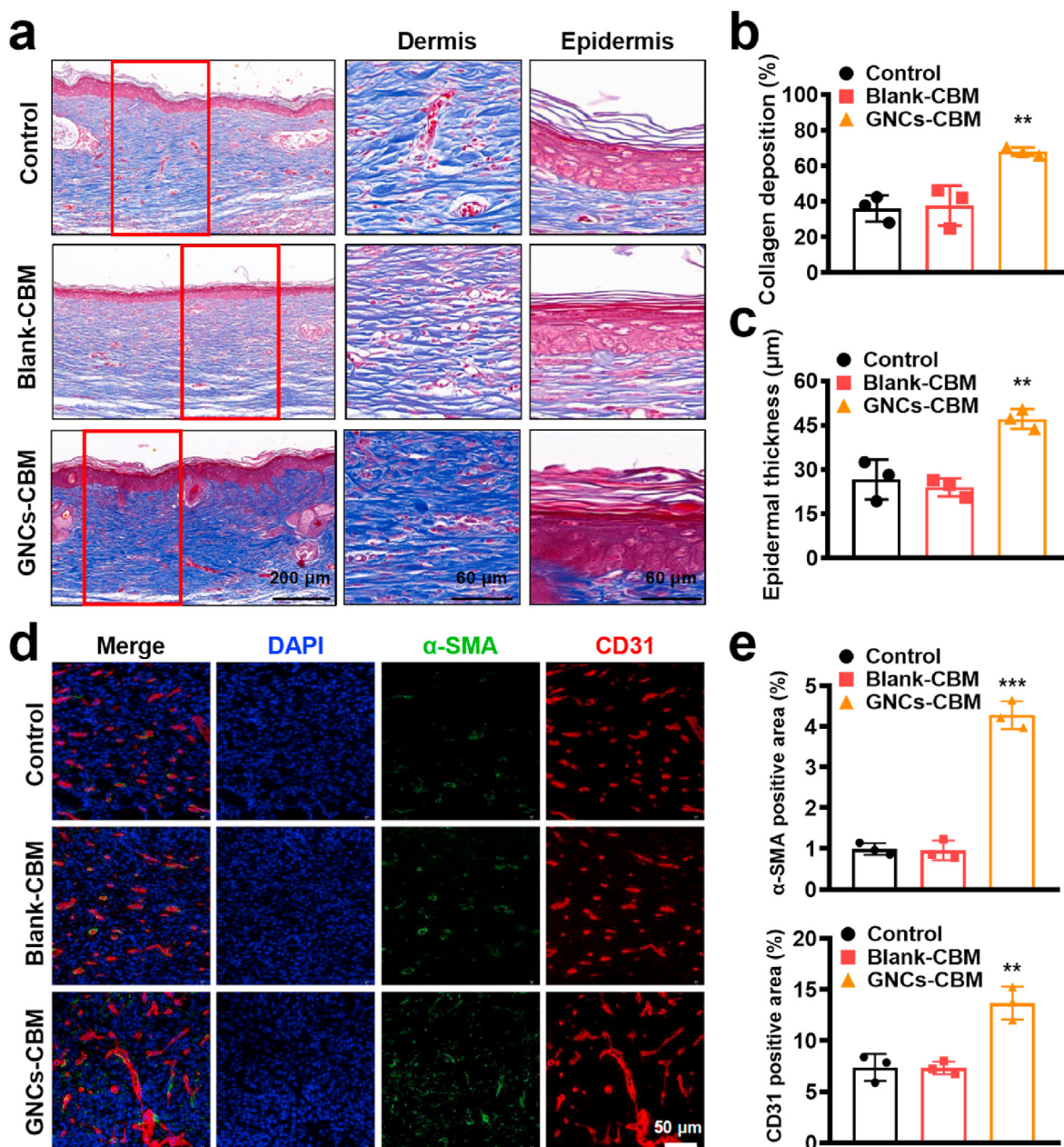
Fig. 8. GNCs-CBM hydrogel promotes the formation of granulation tissues to repair epidermis defects *in vivo*. (a) Masson's staining images of collagen fibers in cross-sectional wound tissues harvested on day 14. Scale bar, 200 μm, 60 μm for enlarged images. (b) Quantification of the areas of stained collagen fibers. (c) Quantification of the average epidermal thickness. (d) Representative immunofluorescence images of α-SMA and CD31 double-stained sections from different groups on day 14. Scale bar, 50 μm. (e) Quantification of the α-SMA-positive areas and CD31-positive areas. $n = 3$, $*p < 0.05$; $**p < 0.01$.

uncovered that GNCs-CBM hydrogel could induce M2 macrophage polarization for resolving inflammation in the early phase of healing and facilitates the transition of the wound into the subsequent proliferative phase.

The Masson staining of the GNCs-CBM group presented significantly more regenerative dense collagen fibers depositing on day 14 compared with that of Blank-CBM and control groups, which were presented with loosened collagens (Fig. 8a). As shown in Fig. 8b, the percentage of collagen deposition area in GNCs-CBM group (67.99 ± 1.36%) was statistically significantly higher than that of control group (38.08 ± 5.90%) and Blank-CBM group (37.71 ± 6.50%). Epidermal thickness at the center of the wound increased significantly in the GNCs-CBM hydrogel groups (47.15 ± 1.93 μm) compared with that of Blank-CBM group (23.17 ± 2.64 μm) and control group (26.67 ± 3.92 μm) (Fig. 8c). Besides, the GNCs-CBM group possessed substantial higher blood vessel

densities at the late stages of wound healing (Fig. 8d), which was supported by the quantitative result of double immunofluorescence staining with CD31 and α-SMA (Fig. 8e). All the above results suggest that GNCs-CBM hydrogel can be potentially used for infected wound therapy *in vivo*.

4. Conclusion

In conclusion, the injectable self-organizing GNCs-CBM hydrogel crosslinked by dimeric H-bonds was prepared to overcome the predicament of infected skin wounds healing. The synthesized MHA-GNCs with the amphiphilic feature played both 1) a structural role in hydrogen bonding with the carbomer to increase the viscosity of the hydrogel as an ideal wound dressing, and 2) a functional role in providing excellent bactericidal activity and anti-inflammatory property for accelerating wound healing. Infected wound healing experiments verified the

excellent anti-infection and immunomodulatory activities of GNCs-CBM hydrogel, which markedly potentiated the wound closure process and the deposition of collagen. These results verify our strategy of increasing the antibacterial activity of GNCs by keeping them at a high protonation level. We envision that the GNCs-CBM hydrogel with antibacterial and immunomodulatory function has a promising prospect as a wound dressing for infected wound healing.

Credit author statement

Zesong Ruan: Conceptualization, Methodology, Visualization, Investigation, Formal analysis, Writing - original draft. Chunlei Zhang: Conceptualization, Investigation, Formal analysis, Writing - Review & Editing, Tingwang Shi: Conceptualization, Methodology, Investigation, Formal analysis. Zhiyuan Luo: Methodology, Investigation. Yuna Zhang: Methodology, Investigation. Zanxia Cao: Software, Formal analysis. Rentai Huang: Methodology, Investigation. Yunfeng Chen: Writing - Review & Editing, Supervision, Project administration, Funding acquisition. Daxiang Cui: Supervision, Funding acquisition.

Declaration of competing interest

The authors declare that they have no known competing financial interests or personal relationships that could have appeared to influence the work reported in this paper.

Acknowledgements

Appendix A. Supplementary data

Supplementary data to this article can be found online at https://doi.org/10.1016/j.mtbio.2022.100426.

References

[1] X. Zhao, H. Wu, B. Guo, R. Dong, Y. Qiu, P.X. Ma, Antibacterial anti-oxidant electroactive injectable hydrogel as self-healing wound dressing with hemostasis and adhesiveness for cutaneous wound healing, Biomaterials 122 (2017) 34–47, https://doi.org/10.1016/j.biomaterials.2017.01.011.

[2] J. Wang, M. Windbergs, Functional electrospun fibers for the treatment of human skin wounds, Eur. J. Pharm. Biopharm. 119 (2017) 283–299, https://doi.org/10.1016/j.ejpb.2017.07.001.

[3] E.S. Chambers, M. Vukmanovic-Stejic, Skin barrier immunity and ageing, Immunology 160 (2) (2020) 116–125, https://doi.org/10.1111/imm.13152.

[4] G. Daeschlein, Antimicrobial and antiseptic strategies in wound management, Int. Wound J. 10 (Suppl 1) (2013) 9–14, https://doi.org/10.1111/iwj.12175.

[5] S. Roy, S. Santra, A. Das, S. Dixith, M. Sinha, S. Ghatak, N. Ghosh, P. Banerjee, S. Khanna, S. Mathew-Steiner, P.D. Ghatak, B.N. Blackstone, H.M. Powell, V.K. Bergdall, D.J. Wozniak, C.K. Sen, Staphylococcus aureus biofilm infection compromises wound healing by causing deficiencies in granulation tissue collagen, Ann. Surg. 271 (6) (2020) 1174–1185, https://doi.org/10.1097/sla.0000000000003053.

[6] L.M. Streicher, Exploring the future of infectious disease treatment in a post-antibiotic era: a comparative review of alternative therapeutics, J. Global Antimicrob. Resist. 24 (2021) 285–295, https://doi.org/10.1016/j.jgar.2020.12.025.

[7] G. Chu, C. Zhang, Y. Liu, Z. Cao, L. Wang, Y. Chen, W. Zhou, G. Gao, K. Wang, D. Cui, A gold nanocluster constructed mixed-metal metal-organic network film for combating implant-associated infections, ACS Nano 14 (11) (2020) 15633–15645, https://doi.org/10.1021/acsnano.0c06446.

[8] J.H. Kwon, W.G. Powderly, The post-antibiotic era is here, Science 373 (6554) (2021) 471, https://doi.org/10.1126/science.abl5997.

[9] A. Gupta, S. Mumtaz, C.H. Li, I. Hussain, V.M. Rotello, Combatting antibiotic-resistant bacteria using nanomaterials, Chem. Soc. Rev. 48 (2) (2019) 415–427, https://doi.org/10.1039/c7cs00748e.

[10] J.M.V. Makabenta, A. Nabawy, C.H. Li, S. Schmidt-Malan, R. Patel, V.M. Rotello, Nanomaterial-based therapeutics for antibiotic-resistant bacterial infections, Nat. Rev. Microbiol. 19 (1) (2021) 23–36, https://doi.org/10.1038/s41579-020-0420-1.

[11] M. Natan, E. Banin, From Nano to Micro: using nanotechnology to combat microorganisms and their multidrug resistance, FEMS Microbiol. Rev. 41 (3) (2017) 302–322, https://doi.org/10.1093/femsre/fux003.

[12] M. AlMatar, E.A. Makky, I. Var, F. Koksal, The role of nanoparticles in the inhibition of multidrug-resistant bacteria and biofilms, Curr. Drug Deliv. 15 (4) (2018) 470–484, https://doi.org/10.2174/1567201815666171207163504.

[13] Z. Qiao, J. Zhang, X. Hai, Y. Yan, W. Song, S. Bi, Recent advances in templated synthesis of metal nanoclusters and their applications in biosensing, bioimaging and theranostics, Biosens. Bioelectron. 176 (2021), 112898, https://doi.org/10.1016/j.bios.2020.112898.

[14] X. Du, R. Jin, Atomically precise metal nanoclusters for catalysis, ACS Nano 13 (7) (2019) 7383–7387, https://doi.org/10.1021/acsnano.9b04533.

[15] A.K. Sharma, S. Pandey, N. Sharma, H.F. Wu, Synthesis of fluorescent molybdenum nanoclusters at ambient temperature and their application in biological imaging, Mater. Sci. Eng., C 99 (2019) 1–11, https://doi.org/10.1016/j.msec.2019.01.029.

[16] A. Ghosh, O.F. Mohammed, O.M. Bakr, Atomic-level doping of metal clusters, Acc. Chem. Res. 51 (12) (2018) 3094–3103, https://doi.org/10.1021/acs.accounts.8b00412.

[17] M.F. Matus, H. Häkkinen, Atomically precise gold nanoclusters: towards an optimal biocompatible system from a theoretical-experimental strategy, Small 17 (27) (2021), e2005499, https://doi.org/10.1002/smll.202005499.

[18] X. Song, W. Zhu, X. Ge, R. Li, S. Li, X. Chen, J. Song, J. Xie, X. Chen, H. Yang, A new class of NIR-II gold nanocluster-based protein biolabels for in vivo tumor-targeted imaging, Angew. Chem. Int. Ed. 60 (3) (2021) 1306–1312, https://doi.org/10.1002/anie.202010870.

[19] Y. Zheng, L. Lai, W. Liu, H. Jiang, X. Wang, Recent advances in biomedical applications of fluorescent gold nanoclusters, Adv. Colloid Interface Sci. 242 (2017) 1–16, https://doi.org/10.1016/j.cis.2017.02.005.

[20] K. Zheng, M.I. Setyawati, D.T. Leong, J. Xie, Overcoming bacterial physical defenses with molecule-like ultrasmall antimicrobial gold nanoclusters, Bioact. Mater. 6 (4) (2021) 941–950, https://doi.org/10.1016/j.bioactmat.2020.09.026.

[21] L. Wang, S. Li, J. Yin, J. Yang, Q. Li, W. Zheng, S. Liu, X. Jiang, The density of surface coating can contribute to different antibacterial activities of gold nanoparticles, Nano Lett. 20 (7) (2020) 5036–5042, https://doi.org/10.1021/acs.nanolett.0c01196.

[22] Y. Xie, Y. Liu, J. Yang, Y. Liu, F. Hu, K. Zhu, X. Jiang, Gold nanoclusters for targeting methicillin-resistant Staphylococcus aureus in vivo, Angew. Chem. Int. Ed. 57 (15) (2018) 3958–3962, https://doi.org/10.1002/anie.201712878.

[23] K. Zheng, M.I. Setyawati, D.T. Leong, J. Xie, Overcoming bacterial physical defenses with molecule-like ultrasmall antimicrobial gold nanoclusters, Bioact. Mater. 6 (4) (2021) 941–950, https://doi.org/10.1016/j.bioactmat.2020.09.026.

[24] Komal Sonia, S. Kukreti, M. Kaushik, Gold nanoclusters: an ultrasmall platform for multifaceted applications, Talanta 234 (2021), 122623, https://doi.org/10.1016/j.talanta.2021.122623.

[25] H. Liang, J. Xu, Y. Liu, J. Zhang, W. Peng, J. Yan, Z. Li, Q. Li, Optimization of hydrogel containing toluidine blue O for photodynamic therapy by response surface methodology, J. Photochem. Photobiol., B 173 (2017) 389–396, https://doi.org/10.1016/j.jphotobiol.2017.06.019.

[26] Y. Huang, F. Shi, L. Wang, Y. Yang, B.M. Khan, K.-L. Cheong, Y. Liu, Preparation and evaluation of Bletilla striata polysaccharide/carboxymethyl chitosan/Carbomer 940 hydrogel for wound healing, Int. J. Biol. Macromol. 132 (2019) 729–737, https://doi.org/10.1016/j.ijbiomac.2019.03.157.

[27] Y. Maslii, O. Ruban, G. Kasparaviciene, Z. Kalveniene, A. Materiienko, L. Ivanauskas, A. Mazurkeviciute, D.M. Kopustinskiene, J. Bernatoniene, The influence of pH values on the rheological, textural and release properties of Carbomer Polacril® 40P-based dental gel formulation with plant-derived and synthetic active components, Molecules 25 (21) (2020), https://doi.org/10.3390/molecules25215018.

[28] V.V. Khutoryanskiy, Hydrogen-bonded interpolymer complexes as materials for pharmaceutical applications, Int. J. Pharm. 334 (1) (2007) 15–26, https://doi.org/10.1016/j.ijpharm.2007.01.037.

[29] H. Van Nguyen, V.H. Nguyen, B.J. Lee, Dual release and molecular mechanism of bilayered aceclofenac tablet using polymer mixture, Int. J. Pharm. 515 (1–2) (2016) 233–244, https://doi.org/10.1016/j.ijpharm.2016.10.021.

[30] J. Lin, E. Pozharski, M.A. Wilson, Short carboxylic acid-carboxylate hydrogen bonds can have fully localized protons, Biochemistry 56 (2) (2017) 391–402, https://doi.org/10.1021/acs.biochem.6b00906.

[31] S. Zhou, L. Wang, Unraveling the structural and chemical features of biological short hydrogen bonds, Chem. Sci. 10 (33) (2019) 7734–7745, https://doi.org/10.1039/c9sc01496a.

[32] D.B. Gurevich, C.E. Severn, C. Twomey, A. Greenhough, J. Cash, A.M. Toye, H. Mellor, P. Martin, Live imaging of wound angiogenesis reveals macrophage orchestrated vessel sprouting and regression, EMBO J. 37 (13) (2018), e97786, https://doi.org/10.15252/embj.201797786.

[33] V. Brancaleone, T. Gobbetti, N. Cenac, P. le Faouder, B. Colom, R.J. Flower, N. Vergnolle, S. Nourshargh, M. Perretti, A vasculo-protective circuit centered on lipoxin A4 and aspirin-triggered 15-epi-lipoxin A4 operative in murine microcirculation, Blood 122 (4) (2013) 608–617, https://doi.org/10.1182/blood-2013-04-496661.

[34] K.L. Spiller, S. Nassiri, C.E. Witherel, R.R. Anfang, J. Ng, K.R. Nakazawa, T. Yu, G. Vunjak-Novakovic, Sequential delivery of immunomodulatory cytokines to facilitate the M1-to-M2 transition of macrophages and enhance vascularization of

bone scaffolds, Biomaterials 37 (2015) 194–207, https://doi.org/10.1016/j.biomaterials.2014.10.017.

[35] S. Lin, Z. Zhou, C. Xu, F. Zeng, Z. Shi, J. Sun, X. Mei, C. Liu, D. Li, Cytokine regulation and fast inflammation resolution in early rheumatoid arthritis by cerium-modified gold nanoclusters, ACS Appl. Mater. Interfaces 14 (16) (2022) 18053–18063, https://doi.org/10.1021/acsami.1c22831.

[36] Z. Zhou, D. Li, X. Fan, Y. Yuan, H. Wang, D. Wang, X. Mei, Gold nanoclusters conjugated berberine reduce inflammation and alleviate neuronal apoptosis by mediating M2 polarization for spinal cord injury repair, Regener. Biomater. 9 (2021), https://doi.org/10.1093/rb/rbab072.

[37] E.L. Wu, X. Cheng, S. Jo, H. Rui, K.C. Song, E.M. Davila-Contreras, Y. Qi, J. Lee, V. Monje-Galvan, R.M. Venable, J.B. Klauda, W. Im, CHARMM-GUI Membrane Builder toward realistic biological membrane simulations, J. Comput. Chem. 35 (27) (2014) 1997–2004, https://doi.org/10.1002/jcc.23702.

[38] S. Jo, T. Kim, V.G. Iyer, W. Im, CHARMM-GUI: a web-based graphical user interface for CHARMM, J. Comput. Chem. 29 (11) (2008) 1859–1865, https://doi.org/10.1002/jcc.20945.

[39] K. Van Raemdonck, S. Umar, K. Palasiewicz, S. Volkov, M.V. Volin, S. Arami, H.J. Chang, B. Zanotti, N. Sweiss, S. Shahrara, CCL21/CCR7 signaling in macrophages promotes joint inflammation and Th17-mediated osteoclast formation in rheumatoid arthritis, Cell. Mol. Life Sci. 77 (7) (2020) 1387–1399, https://doi.org/10.1007/s00018-019-03235-w.

[40] Y. Mao, B. Wang, X. Xu, W. Du, W. Li, Y. Wang, Glycyrrhizic acid promotes M1 macrophage polarization in murine bone marrow-derived macrophages associated with the activation of JNK and NF-κB, Mediat. Inflamm. (2015), 372931, https://doi.org/10.1155/2015/372931, 2015.

[41] H. Yang, L. Song, B. Sun, D. Chu, L. Yang, M. Li, H. Li, Y. Dai, Z. Yu, J. Guo, Modulation of macrophages by a paeoniflorin-loaded hyaluronic acid-based hydrogel promotes diabetic wound healing, Mater. Today Bio 12 (2021), 100139, https://doi.org/10.1016/j.mtbio.2021.100139.

[42] X. Yuan, B. Zhang, Z. Luo, Q. Yao, D.T. Leong, N. Yan, J. Xie, Balancing the rate of cluster growth and etching for gram-scale synthesis of thiolate-protected Au$_{25}$ nanoclusters with atomic precision, Angew. Chem. Int. Ed. 53 (18) (2014) 4623–4627, https://doi.org/10.1002/anie.201311177.

[43] V. Rubio-Giménez, S. Tatay, F. Volatron, F.J. Martínez-Casado, C. Martí-Gastaldo, E. Coronado, High-quality metal-organic framework ultrathin films for electronically active interfaces, J. Am. Chem. Soc. 138 (8) (2016) 2576–2584, https://doi.org/10.1021/jacs.5b09784.

[44] E.G. Palacios, G. Juárez-López, A.J. Monhemius, Infrared spectroscopy of metal carboxylates: II. Analysis of Fe(III), Ni and Zn carboxylate solutions, Hydrometallurgy 72 (1) (2004) 139–148, https://doi.org/10.1016/S0304-386X(03)00137-3.

[45] R.B. Viana, A.B. da Silva, A.S. Pimentel, Adsorption of sodium dodecyl sulfate on Ge substrate: the effect of a low-polarity solvent, Int. J. Mol. Sci. 13 (7) (2012) 7980–7993, https://doi.org/10.3390/ijms13077980.

[46] A.M. Intlekofer, B. Wang, H. Liu, H. Shah, C. Carmona-Fontaine, A.S. Rustenburg, S. Salah, M.R. Gunner, J.D. Chodera, J.R. Cross, C.B. Thompson, L-2-Hydroxyglutarate production arises from noncanonical enzyme function at acidic pH, Nat. Chem. Biol. 13 (5) (2017) 494–500, https://doi.org/10.1038/nchembio.2307.

[47] H. Yamamura, T. Hagiwara, Y. Hayashi, K. Osawa, H. Kato, T. Katsu, K. Masuda, A. Sumino, H. Yamashita, R. Jinno, M. Abe, A. Miyagawa, Antibacterialactivity of

[48] membrane-permeabilizing bactericidal cyclodextrin derivatives, ACS Omega 6 (47) (2021) 31831–31842, https://doi.org/10.1021/acsomega.1c04541.

[48] R. Kumari, R. Kumar, C. Open, Source Drug Discovery, A. Lynn, g_mmpbsa–a GROMACS tool for high-throughput MM-PBSA calculations, J. Chem. Inf. Model. 54 (7) (2014) 1951–1962, https://doi.org/10.1021/ci500020m.

[49] H. Cheng, M. Byrska-Bishop, C.T. Zhang, C.J. Kastrup, N.S. Hwang, A.K. Tai, W.W. Lee, X. Xu, M. Nahrendorf, R. Langer, D.G. Anderson, Stem cell membrane engineering for cell rolling using peptide conjugation and tuning of cell–selectin interaction kinetics, Biomaterials 33 (20) (2012) 5004–5012, https://doi.org/10.1016/j.biomaterials.2012.03.065.

[50] R.E. Unger, K. Peters, A. Sartoris, C. Freese, C.J. Kirkpatrick, Human endothelial cell-based assay for endotoxin as sensitive as the conventional Limulus Amebocyte Lysate assay, Biomaterials 35 (10) (2014) 3180–3187, https://doi.org/10.1016/j.biomaterials.2013.12.059.

[51] H. Qiu, F. Pu, Z. Liu, Q. Deng, P. Sun, J. Ren, X. Qu, Depriving bacterial adhesion-related molecule to inhibit biofilm formation using CeO$_2$-decorated metal-organic frameworks, Small 15 (36) (2019), e1902522, https://doi.org/10.1002/smll.201902522.

[52] S.R. Park, A. Tripathi, J. Wu, P.J. Schultz, I. Yim, T.J. McQuade, F. Yu, C.-J. Arevang, A.Y. Mensah, G. Tamayo-Castillo, C. Xi, D.H. Sherman, Discovery of cahuitamycins as biofilm inhibitors derived from a convergent biosynthetic pathway, Nat. Commun. 7 (2016), https://doi.org/10.1038/ncomms10710, 10710-10710.

[53] H. Sun, Q. Zhang, R. Wang, H. Wang, Y.T. Wong, M. Wang, Q. Hao, A. Yan, R.Y. Kao, P.L. Ho, H. Li, Resensitizing carbapenem- and colistin-resistant bacteria to antibiotics using auranofin, Nat. Commun. 11 (1) (2020) 5263, https://doi.org/10.1038/s41467-020-18939-y.

[54] T. Wang, I. El Meouche, M.J. Dunlop, Bacterial persistence induced by salicylate via reactive oxygen species, Sci. Rep. 7 (2017), 43839, https://doi.org/10.1038/srep43839.

[55] T. Shi, Z. Ruan, X. Wang, X. Lian, Y. Chen, Erythrocyte membrane-enveloped molybdenum disulfide nanodots for biofilm elimination on implants via toxin neutralization and immune modulation, J. Mater. Chem. B 10 (11) (2022) 1805–1820, https://doi.org/10.1039/D1TB02615A.

[56] T. Li, M. Peng, Z. Yang, X. Zhou, Y. Deng, C. Jiang, M. Xiao, J. Wang, 3D-printed IFN-γ-loading calcium silicate-β-tricalcium phosphate scaffold sequentially activates M1 and M2 polarization of macrophages to promote vascularization of tissue engineering bone, Acta Biomater. 71 (2018) 96–107, https://doi.org/10.1016/j.actbio.2018.03.012.

[57] S. Hao, J. Meng, Y. Zhang, J. Liu, X. Nie, F. Wu, Y. Yang, C. Wang, N. Gu, H. Xu, Macrophage phenotypic mechanomodulation of enhancing bone regeneration by superparamagnetic scaffold upon magnetization, Biomaterials 140 (2017) 16–25, https://doi.org/10.1016/j.biomaterials.2017.06.013.

[58] R.A. Dorschner, J. Lee, O. Cohen, T. Costantini, A. Baird, B.P. Eliceiri, ECRG4 regulates neutrophil recruitment and CD44 expression during the inflammatory response to injury, Sci. Adv. 6 (11) (2020), https://doi.org/10.1126/sciadv.aay0518 eaay0518.

[59] Z. Fan, J. Deng, P.Y. Li, D.R. Chery, Y. Su, P. Zhu, T. Kambayashi, E.P. Blankenhorn, L. Han, H. Cheng, A new class of biological materials: cell membrane-derived hydrogel scaffolds, Biomaterials 197 (2019) 244–254, https://doi.org/10.1016/j.biomaterials.2019.01.020.